Journal Pre-proof

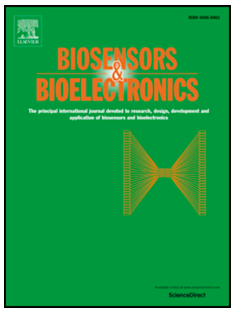

Sub-picomolar lateral flow antigen detection with two-wavelength imaging of composite nanoparticles

Benjamin S. Miller, Michael R. Thomas, Matthew Banner, Jeongyun Kim, Yiyun Chen, Qingshan Wei, Derek K. Tseng, Zoltán S. Göröcs, Aydogan Ozcan, Molly M. Stevens, Rachel A. McKendry

PII: S0956-5663(22)00173-7

DOI: https://doi.org/10.1016/j.bios.2022.114133

Reference: BIOS 114133

To appear in: *Biosensors and Bioelectronics*

Received Date: 21 October 2021

Revised Date: 2 February 2022

Accepted Date: 22 February 2022

Please cite this article as: Miller, B.S., Thomas, M.R., Banner, M., Kim, J., Chen, Y., Wei, Q., Tseng, D.K., Göröcs, Zoltá.S., Ozcan, A., Stevens, M.M., McKendry, R.A., Sub-picomolar lateral flow antigen detection with two-wavelength imaging of composite nanoparticles, *Biosensors and Bioelectronics* (2022), doi: https://doi.org/10.1016/j.bios.2022.114133.

CRediT authorship contribution statement

Benjamin S. Miller: conceptualization of the study, experimental planning, carrying out lateral flow and imaging experiments, data analysis. **Michael R. Thomas:** conceptualization of the study, experimental planning, carrying out lateral flow and particle conjugation experiments, data analysis. **Matthew Banner:** data analysis. **Jeongyun Kim:** carrying out particle conjugation experiments. **Yiyun Chen:** experimental planning, carrying out particle conjugation experiments, TEM and DLS characterisation. **Qingshan Wei:** conceptualization of the study, experimental planning, data analysis. **Derek K. Tseng:** conceptualization of the study, device design. **Zoltán S. Göröcs:** conceptualization of the study, experimental planning. **Aydogan Ozcan:** conceptualization of the study, data analysis. Molly **M. Stevens:** conceptualization of the study, experimental planning. **Rachel A. McKendry:** conceptualization of the study, experimental planning, data analysis.

Sub-picomolar lateral flow antigen detection with two-wavelength imaging of composite nanoparticles

Benjamin S. Miller[a,b], Michael R. Thomas[a,c], Matthew Banner[a,d], Jeongyun Kim[c], Yiyun Chen[c], Qingshan Wei[e,f], Derek K. Tseng[e], Zoltán S. Göröcs[e], Aydogan Ozcan[e], Molly M. Stevens[c] and Rachel A. McKendry[a,b,*]

a. London Centre for Nanotechnology, University College London, 17-19 Gordon Street, London, WC1H 0AH, United Kingdom
b. Division of Medicine, University College London, Gower Street London WC1E 6BT, United Kingdom
c. Department of Materials, Department of Bioengineering and Institute of Biomedical Engineering, Imperial College London, London SW7 2BP, United Kingdom
d. Department of Biochemical Engineering, University College London, Bernard Katz Building, Gower Street, London, WC1E 6BT
e. Electrical and Computer Engineering Department, University of California, Los Angeles, Los Angeles, CA, USA
f. Department of Chemical and Biomolecular Engineering, North Caroline State University, Raleigh NC, USA

Keywords

lateral flow
imaging
nanoparticles
biosensors

Abstract

Lateral flow tests, commonly based on metal plasmonic nanoparticles, are rapid, robust, and low-cost. However, improvements in analytical sensitivity are required to allow detection of low-abundance biomarkers, for example detection of low antigen concentrations for earlier or asymptomatic diagnosis of infectious diseases. Efforts to improve sensitivity often require changes to the assay. Here, we developed optical methods to improve the sensitivity of absorption-based lateral flow tests, requiring no assay modifications to existing tests. We experimentally compared five different lock-in and subtraction-based methods, exploiting the narrow plasmonic peak of gold nanoparticles for background removal by imaging at different light wavelengths. A statistical framework and three fitting models were used to compare limits of detection, giving a 2.0-5.4-fold improvement. We then demonstrated the broad applicability of the method to an ultrasensitive assay, designing 530 nm composite nanoparticles to increase the particle volume, and therefore light absorption per particle, whilst retaining the plasmonic peak to allow background removal and without adding any assay steps. This multifaceted, modular approach gave a combined 58-fold improvement in the fundamental limit of detection using a biotin-avidin model over 50 nm gold nanoparticles with single-wavelength imaging. Applying to a sandwich assay for the detection of HIV capsid protein gave a limit of detection of 170 fM. Additionally, we developed an open-source software tool for performing the detection limit analysis used in this work.

1 Introduction

Infectious diseases represent an enormous global health challenge in our increasingly connected world. The ongoing COVID-19 pandemic has seen 272 million confirmed cases and 5.3 million deaths worldwide at the time of writing (World Health Organization, 2021), and caused enormous economic damage (The World Bank, 2020). The HIV pandemic has seen 76 million infections, causing almost 33 million deaths as of 2019 (UNAIDS, 2020). Early detection is crucial to reducing the impact of infectious disease outbreaks, helping to both reduce spread by informing action to prevent onwards transmission – 7.1 million people living with HIV are unaware of their status (UNAIDS, 2020), around one quarter of SARS-CoV-2 infections are asymptomatic (Buitrago-Garcia et al., 2020); and improve individual patient prognosis from earlier treatment (May et al., 2011).

Absorption based lateral flow assays (LFAs) are among the most common tests used worldwide. They are low-cost, easy-to-use, including for self-testing, and can be read by eye, or by a camera or smartphone with (Mudanyali et al., 2012) or without a dedicated reader (Loynachan et al., 2018), eliminating the need for external equipment (World Health Organization, 2012). However, the sensitivity of these tests remains a key challenge, with many unable to detect low levels of biomarkers needed for early detection of infectious diseases. This has been emphasised by the low reported sensitivities of SARS-CoV-2 LFAs (The University of Liverpool, 2020).

Ngom et al. (Ngom et al., 2010) found that 75% of LFAs used colloidal gold nanoparticle (AuNP) labels. The sensitivity of these tests is limited by the absorption per particle, and the variation of the nitrocellulose background (due to its porous structure), which can mask faint test lines generated by low levels of biomarkers. The absorption of AuNPs is related to their size, which is limited by two factors: AuNPs become less stable, and therefore more difficult to functionalise above diameters of ~40-50 nm (Laitinen and Vuento, 1996); secondly when the diameter of AuNPs increases above ~100 nm the plasmonic absorption peak broadens, limiting peak absorption (Cytodiagnostics, n.d.; Link and El-Sayed, 1999).

Various strategies have been used to improve the sensitivity of AuNP-based assays by increasing the absorption of the labels, including binding multiple AuNPs using a secondary antibody (Rivas et al., 2015), binding AuNP aggregates (Hu et al., 2013) and chains (Ruiz-Sanchez et al., 2017) (2.5 and 4-fold improvements in sensitivity, respectively), the use of double-layer gold (Choi et al., 2010) (100-fold improvement), the use of silver (Rodríguez et al., 2016) (3-fold improvement) and gold (Fu et al., 2012) (4-fold improvement) ion deposition for signal enhancement, and AuNP-patterned magnetic nanoparticles (Tang et al., 2009) (3-fold improvement over AuNPs). Thermal contrast imaging gave an 8-fold improvement over conventional optical imaging (Wang et al., 2016). Evans et al. impregnated paper membranes with silica nanoparticles to improve colour uniformity, reporting a 2-fold improvement (Evans et al., 2014). However, these methods require significant changes to the assay, extra steps, or specific readout equipment. In addition, enzymatic nanoparticles have been used to amplify readout (Loynachan et al., 2018), but require an additional step.

The narrow plasmonic absorption peak of 50 nm AuNPs contrasts the absorption of the nitrocellulose paper LFA substrate, which absorbs uniformly over a broad frequency range. This work aims to exploit this difference to investigate a variety of light frequency-based methods for improving the signal-to-noise ratio by background removal, applicable to existing LFAs without changing the assay. Improvements in signal-to-noise ratio should translate into improvements in limits of detection (analytical sensitivity). Although to the best of our knowledge this is the first time this approach has been applied to adsorption-based LFAs, ratiometric methods are widely used (Huang et al., 2018), including a similar method in a fluorescence-mode LFA with quantum dots, which allowed imaging

without optical filters, successfully reducing the excitation intensity variability (Shah et al., 2018). Bond et al. (Bond et al., 2013) also used transmission measurements with red and green light emitting diodes (LEDs), subtracting the two extinction coefficients to measure haemoglobin levels in blood spots on paper.

In this work the use of image subtraction, and three other techniques using light wavelength modulation to employ frequency-based lock-in amplification (analogous to (Miller et al., 2020)) were investigated to improve the sensitivity of LFAs, without requiring any modifications to the test itself. This would allow integration into existing rapid testing workflows. This method was then extended to three plasmonic nanoparticle types, including a composite particle approach, to further improve sensitivity. Fundamental limits of detection (LODs) were quantified using a biotin-avidin model assay, and the best system was applied to an HIV diagnostic, detecting the p24 capsid protein.

2 Material and methods

2.1 Nanoparticle synthesis and conjugation

2.1.1 PS-AuNP preparation

250 µL of a 0.15 wt% solution of cationic amine-terminated polystyrene nanoparticles (Ikerlat Polymers) in water in a glass vial. This was diluted with 2,250 µL of distilled water. 2,500 µL of citrate-capped 14.5 nm gold nanoparticles were added rapidly with mixing and incubated at room temperature for 1.5 hr to yield polystyrene nanoparticles decorated with gold nanoparticles (PS-AuNPs). Aliquots were taken for subsequent modification.

2.1.2 Biotin-conjugated PS-AuNPs

A 1 mL aliquot of the PS-AuNPs was mixed with 250 µL of 1 mg/mL BSA in PBS was added and incubated for 1 hr at room temperature on a microcentrifuge tube shaker at 500 rpm. The particles were washed twice by centrifugation at 1,000 rcf for 10 min (an initial resuspension in 1 mL of milli-Q followed by a final resuspension in 200 µL). To this suspension, 2 µL of 50 mM EZ-Link NHS-PEG12-Biotin (Thermo Fisher Scientific) was added and incubated for 30 min at room temperature on a 500-rpm shaker. Following this, the suspension was washed by centrifugation at 800 rcf (10 min) and resuspension in 0.2 wt% β-casein 0.1 wt% Tween 20 (Sigma-Aldrich) in PBS for 3 wash cycles.

2.1.3 Anti-p24-conjugated PS-AuNPs

A 1 mL aliquot of the PS-AuNPs was mixed with a premixed solution of 100 µL of HEPES 100 mM pH 7.4 and 3 µL of 3.55 mg/mL anti-p24 antibody (Capricorn Products, HIV-018-48303). This mixture was incubated for 1.25 hr at room temperature. Blocking was performed by adding 200 µL of 2 wt% β-casein in PBS to this mixture followed by vortexing. This mixture was left for 2 hr at room temperature. This mixture was then washed by centrifugation (4 washes at 750 rcf for 10 min) and resuspended in 0.1 wt% β-casein, 0.1 vol% Tween 20 in PBS each time. The final resuspension was into 100 µL, and aliquots were combined as necessary for experiments.

2.1.4 Particle characterisation

Particle absorption spectra were measured using a Nanodrop One^{C} (Thermo Fisher Scientific) to check for aggregation and absorption properties. Dynamic light scattering (DLS, Zeta Sizer Nanoseries, Malvern Instruments, Ltd.) was used to characterise the hydrodynamic diameter and monodispersity of nanoparticles. Monodispersity was also measured by imaging the fluorescence of the PS particles using a microscope (Olympus BX-51). Samples for transmission electron miscroscopy (TEM) were prepared by drop casting the BSA-biotin PS-AuNPs to a TEM copper grid (CF-400-Cu, Electron Microscopy Sciences) which was then dried in air for 30 min. Nanoparticle TEM samples were imaged

on a JEOL 2100F Transmission Electron Microscope at 200 kV with a beam current of 101 μA}. TEM micrographs were captured with the Gatan Orius SC1000 camera at magnifications of 25,000x and 60,000x.

2.2 LFA procedure

2.2.1 Biotin-avidin model

Biotinylated 50 and 100 nm AuNPs (Sigma-Aldrich) were serially-diluted in running buffer (PBS, 5 wt% BSA 0.05 vol% Tween 20 (Sigma-Aldrich)). PS-AuNPs were diluted in 0.2 wt% β-casein 0.1 wt% Tween 20 (Sigma-Aldrich) in PBS. 50 μL of resulting suspensions were run on LFAs, printed with poly-streptavidin test lines (Mologic).

2.2.2 HIV capsid antigen detection

A serial dilution of p24 antigen was performed in a pseudo-serum buffer (fetal bovine serum + 0.1 vol% Tween 20). 50 μL of these solutions were mixed with 10 μL of a biotinylated anti-p24 nanobody (Loynachan et al., 2018), and 10 μL of anti-p24-functionalised PS-AuNPs (0.1 nM). The resulting suspensions were run on LFAs, printed with poly-streptavidin test lines (Mologic). After running, 50 μL of wash buffer (PBS, 0.1 wt% β-casein, 0.1 vol% Tween 20) was run on the strips.

2.3 LFA imaging

LFAs were imaged with a microscope (Olympus BX-51) in brightfield reflection mode at a magnification of 5X using a 16-channel LED light source (CoolLED pE-4000) and an sCMOS camera (Hamamatsu ORCA-Flash4.0 V3). Images were taken at under illumination from each of the 16 LEDs. Image capture at different illumination wavelengths was automated using μManager (Edelstein et al., 2014).

To take image sequences under a wavelength-switching light source the light source was controlled using a combination of a PC and a microcontroller (Arduino Nano 3.0). The PC USB 'Virtual Serial Port' interface was used in Matlab to set the LED channels to analogue mode. Two outputs of the microcontroller were then connected to the analogue inputs of the light source via the pE-Expansion Box (CoolLED), one directly, giving the 5V from the microcontroller, and one via a small transistor circuit connected to an analogue voltage source, allowing analogue control of voltage input to the second channel of the light source. This meant the reflected intensity of the two channels can be matched using a blank strip, giving constant intensity whilst switching wavelength. The microcontroller was then programmed to alternate the channels to switch wavelength at a set frequency. HCImage Live (Hamamatsu) was used to capture image sequences of 1200 images at a sampling rate of 20 Hz and an exposure time of 50 ms.

2.4 LOD analysis

Captured images were analysed experimentally by the following five methods:

(1) **Green** Illumination: After capturing single images under 525 nm illumination, images were normalised by flattening the histogram using the `HistrogramTransform` function in Mathematica (Wolfram). Images were then averaged (mean) across their width (perpendicular to the flow) to produce one-dimensional spatial line profiles along the LFA strip (flow direction). To remove vignetting (see Figure 4b), a moving average of the mean of the negative controls was subtracted from all line profiles. The peak heights were then calculated by finding the location of the absolute maximum of the line profile. Different numbers of pixels were averaged around this maximum to give the final peak value (Matlab, Mathworks).

(2) **Subtracted**: two images were taken under 525 and 660 nm illumination for each strip. 525 nm matches the absorption peak for AuNPs, whilst there is little absorption from AuNPs at

660nm. The nitrocellulose background (and negative controls) absorbs approximately uniformly over both wavelengths. The illumination intensities are tuned to keep the imaged intensity of the negative controls equal for the two illumination wavelengths. These resulting images were normalised as above, then subtracted (`ImageSubtract`) to produce a difference image, which was normalised again. Peaks sizes were then quantified as in (1). This procedure is shown schematically in Supplementary Figure 1.

(3) **Lock-in** analysis: 15 s image sequences were captured under wavelength-switching illumination, switching between 525 and 660 nm at a rate of 5 Hz. Due to the AuNP and background absorptions under each wavelength, described above, this appears to cause the test line to flash at 5 Hz, whilst the background remains constant, as shown in the Supplementary Animation. Separating the 5 Hz signal from the constant signal, therefore, separates the AuNP signal from the background, allowing background removal. This was first performed by averaging each image in the sequence to produce a one-dimensional time series. A lock-in algorithm was applied to quantify the amplitude of the 5 Hz (modulation frequency) component of the time series, corresponding to contribution of the AuNPs to the absorption. The lock-in algorithm is described in full by Miller et al. (Miller, 2019; Miller et al., 2020). This procedure is detailed schematically in Supplementary Figure 2.

(4) **Line-wise** lock-in analysis: Image sequences were captured as in (3). Then, each image in the sequences was averaged across its width (perpendicular to the test line) to produce a line profile along the LFA strip at each time point. This is then two-dimensional dataset (one spatial dimension along the strip and time) is then transposed to produce a set of time-series, one for each point along the strip. The lock-in algorithm was then applied to each time-series to produce a lock-in value (representing the magnitude of the 5 Hz AuNP signal) at each point along the LFA strip. These points produce an 'enhanced line profile', which was then analysed as described in (1). This is detailed in Supplementary Figure 3.

(5) **Pixelwise** lock-in analysis: Image sequences were captured as in (3). The three-dimensional dataset was reshaped to produce a set of time-series, one for each pixel of the camera field-of-view. Lock-in analysis was then applied to each time-series to produce a set of lock-in values, one for each pixel. These were then reconstructed into an 'enhanced image', which was analysed as in (1). This is detailed in Supplementary Figure 4.

The same LFA strips were used for the five methods, to compare the data capture methods experimentally without introducing additional variation. The peak sizes from each of these methods were used to calculate the LODs using an extended version of the method presented by Holstein et al. (Holstein et al., 2015). For each of the five data capture methods, three fitting models were compared: the Langmuir adsorption model (Supplementary Equation 1), the four-parameter logistic regression (Supplementary Equation 12), and five-parameter logistic regression (Supplementary Equation 25 (Dunn and Wild, 2013)). Before analysis, log-transformations of concentration and peak size were performed ($\log(\text{Peak Size} + 2)$). The method was also extended to include a G test ('t Lam, 2010) to exclude outlier variances when calculating the average variance for the positive peak sizes. This hypothesis test assumes the variances should be constant, and not vary with signal or concentration. To ensure that the variance was constant, a log transformation was performed to normalise the variance across different signals and concentrations.

2.5 LOD software tool

The software tool was developed using the Matlab App Designer in Matlab 2021a. It includes code from (Brewer, 2021; Cobeldick, 2021; Danz, 2021; Trujillo-Ortiz, 2021a, 2021b)

3 Results and Discussion

An illustration of the principle is shown in Figure 1. Plasmonic nanoparticles, such as gold nanoparticles, are commonly used in LFAs, where they bind via a sandwich assay to the nitrocellulose substrate. Figure 1a shows a sandwich assay used here for the detection of the HIV capsid protein. The accumulation of nanoparticles at the test line generates a coloured line due to the wavelength-specific absorption of plasmonic nanoparticles. In the case of the nanoparticles used here, light is strongly absorbed in the green region, generating a red-coloured test line in the presence of a target biomarker, whilst nitrocellulose absorbs over a broad wavelength-range. In Figure 1b, their respective spectra are plotted along with the 525 and 660 nm LED spectra and the camera quantum efficiency. Multiplying gives the resultant spectra, showing strong absorption under green illumination but not red by the AuNPs, and absorption under both wavelengths by the nitrocellulose. This difference was exploited to remove the background absorption of the nitrocellulose substrate from the images.

The simplest method was performed by imaging under 525 and 660 nm illumination, and taking the difference of the resulting normalised images (Figure 1c). Although higher wavelengths would give slightly lower gold nanoparticle absorption, 660 nm is convenient due to the wider availability of LEDs and camera sensors. This principle was then extended to frequency-based lock-in amplification by using a light source whose wavelength switches between 525 and 660 nm at a fixed modulation frequency of 5 Hz, as shown in Supplementary Figure 2.

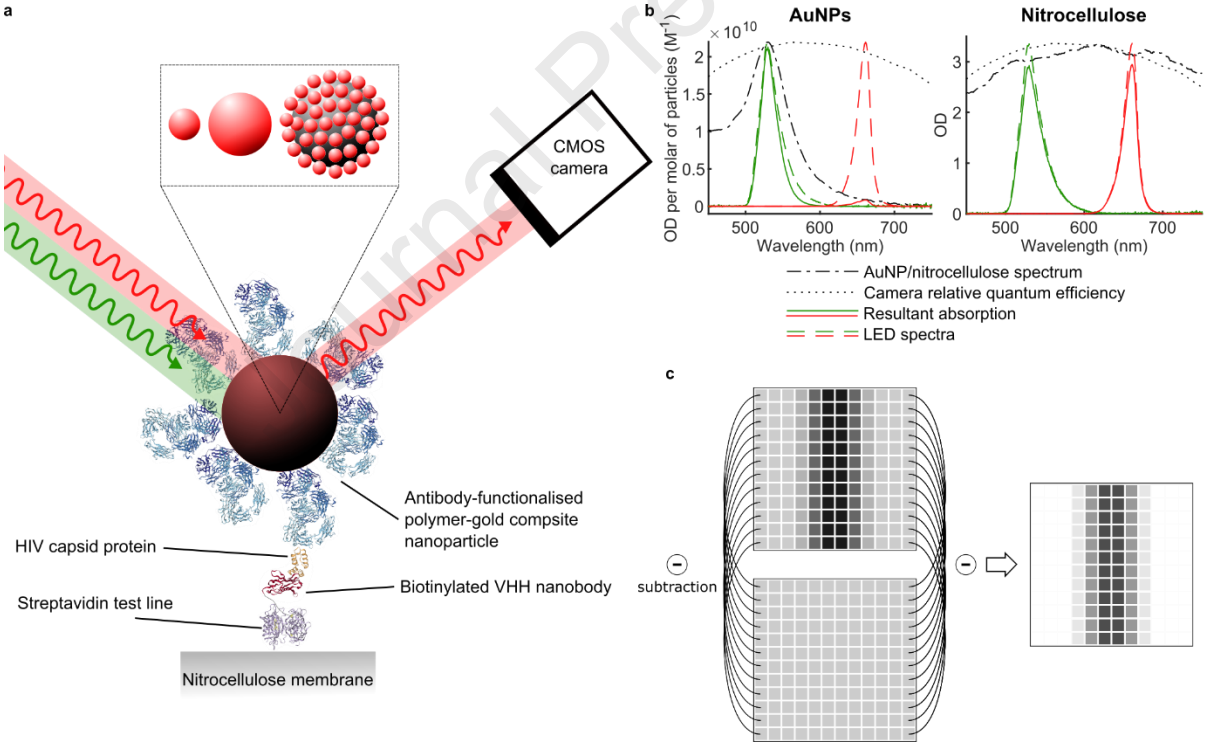

Figure 1: Principle of two-wavelength background subtraction. ***a*** *An illustration of the LFA: plasmonic nanoparticles are immobilised on a nitrocellulose membrane in the presence of the HIV capsid protein. Nanoparticles used in this paper are 50 and 100 nm gold nanoparticles (AuNPs), and 530 nm polystyrene-AuNP composite particles. The strip is imaged under two different light frequencies, both of which are absorbed and reflected similarly by the nitrocellulose, but only one of which is strongly absorbed by the gold nanoparticles, allowing for subtraction of the background by various methods. Modelling of the relative absorption of AuNPs and nitrocellulose under 525 and 660 nm illumination is shown in* ***b****. Multiplying their absorption spectra (dash-dotted lines) by the LED spectra (dashed lines) and the camera quantum efficiency spectrum (dotted lines) gives the relation absorption under each illumination condition (solid lines).* ***c*** *The principle of two-wavelength image subtraction. Two images are taken under two different illumination wavelengths: 525 nm, matching the peak light absorption of AuNPs, and 660 nm,*

where there is minimal absorption from AuNPs. The nitrocellulose background absorbs uniformly at both wavelengths. Pixelwise subtraction of the two images gives a difference image with background and background variation removed, improving signal-to-background ratio, and therefore analytical sensitivity.

3.1 Comparison of data capture methods and fitting models

A biotin-avidin model was used to test the fundamental LODs of five data capture methods in an idealised assay. The high affinity of the biotin-avidin interaction and accessibility of reagents make this an ideal system for benchmarking the performance of classes of nanoparticle, independently of specific assay and binding rate considerations. A serial dilution of 50 nm AuNPs (standard for AuNP LFAs) was run on LFAs, binding directly to a poly-streptividin test line, as shown in Figure 2a. The five data capture methods were tested experimentally on the same LFA strips to remove this as a source of variation. Figure 2b-f shows results of the five data capture methods described in Section 2.4. All the methods measure peak size in the same way from the line profile, which eliminates analysis bias between methods, except (d), where the output from the lock-in analysis is already a single value analogous to peak size.

The LODs for each data capture method were calculated by extending an existing framework (Holstein et al., 2015) to three models: the Langmuir adsorption model (Supplementary Equations 1-11), the four-parameter logistic regression (4PL, Supplementary Equations 12-24), and five-parameter logistic regression (5PL, Supplementary Equations 25-39 (Dunn and Wild, 2013)). These three models were fitted to all five data capture methods, as shown in Supplementary Figure 5. The suitability of the three models was then compared using the root mean squared errors (RMSE) to evaluate goodness of fit; the small-sample corrected Akaike Information Criterion (AICc), which uses the goodness of fit and number of model parameters to choose the best model, considering overfitting and underfitting; and likelihood ratio tests. Fitting model selection was performed by the following steps:

(1) The AICc was used to compare all three fitting models. This is necessary because the Langmuir model is not nested, whilst the likelihood ratio test is only suitable for comparing the nested 4PL and 5PL models. The resulting values are shown in Supplementary Table 1. All three models gave very good RMSEs with all five datasets. The AICc values showed the 4PL to be better than or equal to the other models in four of the five capture methods. For the lock-in method, shown in Figure 2d the 5PL model gave a better AICc, but this was not considered consequential because the RMSE was similar, and this data capture method gives the worst LOD.
(2) The (nested) 4PL and 5PL fitting models were then separately compared for each of the data capture methods using likelihood ratio tests. Likelihood ratio test p-values were non-significant (Supplementary Table 1), indicating that the 5PL is not a significantly better model by goodness of fit so 4PL should be chosen as it uses fewer parameters. This held for all the methods except the lock-in method, agreeing with the AICc values.
(3) We proposed to include a G test ('t Lam, 2010) to exclude outlier variances from the LOD calculation. A comparison of LODs with and without this step is shown in Supplementary Table 2 showing no significant differences between LODs.

As a result of these three comparisons, the 4PL model with a G test was used for all subsequent analysis, including the fits and LODs in Figure 2.

Supplementary Table 3 lists detection limits and confidence intervals corresponding to Figure 2 for each data capture method, along with p-values from two-tailed t-tests comparing to the green illumination single image method. The best LOD is given by the image subtraction method, with an LOD of 16 fM compared to 87 fM for the green illumination; a 5.4-fold improvement (Figure 2g), and a p-value of 7.9×10^{-7} denoting the difference is significant. The subtraction, line-wise and pixelwise

methods give similar LODs, as demonstrated by ANOVA with the Turkey HSD post-hoc test: p-values of 0.65, 0.99 and 0.34 for comparisons of the line-wise and subtraction, pixelwise and line-wise, and pixelwise and subtraction methods. The subtraction method was chosen for simplicity: it does not require a time-varying light source, and is fastest as it requires the capture of only two images.

Despite the similar methods the lock-in has a significantly worse LOD than the line-wise and pixelwise methods. This is because the negative controls give a small background signal (as seen in Supplementary Figure 2a), obscuring low-concentration samples. This is a result of inhomogeneity between nitrocellulose strips, leading to small changes in the relative mean absorption under different illuminations. In the line-wise and pixelwise methods, enhanced line profiles are generated to find the peak size: a differential measurement between the test line and background (nitrocellulose strip). This means this background signal is subtracted, as the lock-in transformation is linear, giving just the test line value. A further comparison was performed between green illumination and greyscale, which is commonly used, shown in Supplementary Figure 6. Greyscale gave a worse LOD than green illumination (116 fM), although the difference is not significant (p-value = 0.34 from two-tailed t-test).

These LOD improvements require no modification to existing tests using plasmonic nanoparticles, allowing for two complementary readout methods: strips can be read by eye under ambient light; and if a reader is present, they can be read in subtraction-mode, improving LOD. The background subtraction also increases the dynamic range by the same factor as the LOD improvement by considering the two linear regions, before and after subtraction.

During image analysis, different number of pixels can be averaged along the strip (perpendicular to the test line), affecting LOD (Supplementary Figure 7). Green illumination analysis gives the best LOD at around 15 pixels, the approximate width of the test line using a biotin-avidin model, as expected. Above this, the LOD worsens, before plateauing at ~150 pixels. This is a trade-off between averaging more pixels to reduce the blank (negative control) variation, and reducing positive test line values by including background pixels in the average. This effect is less evident when using background removal methods, because, although the positive signal is still reduced by averaging more pixels, the more consistent background gives a larger reduction in the variance of the blanks, reducing the cutoff, so the LOD is less affected.

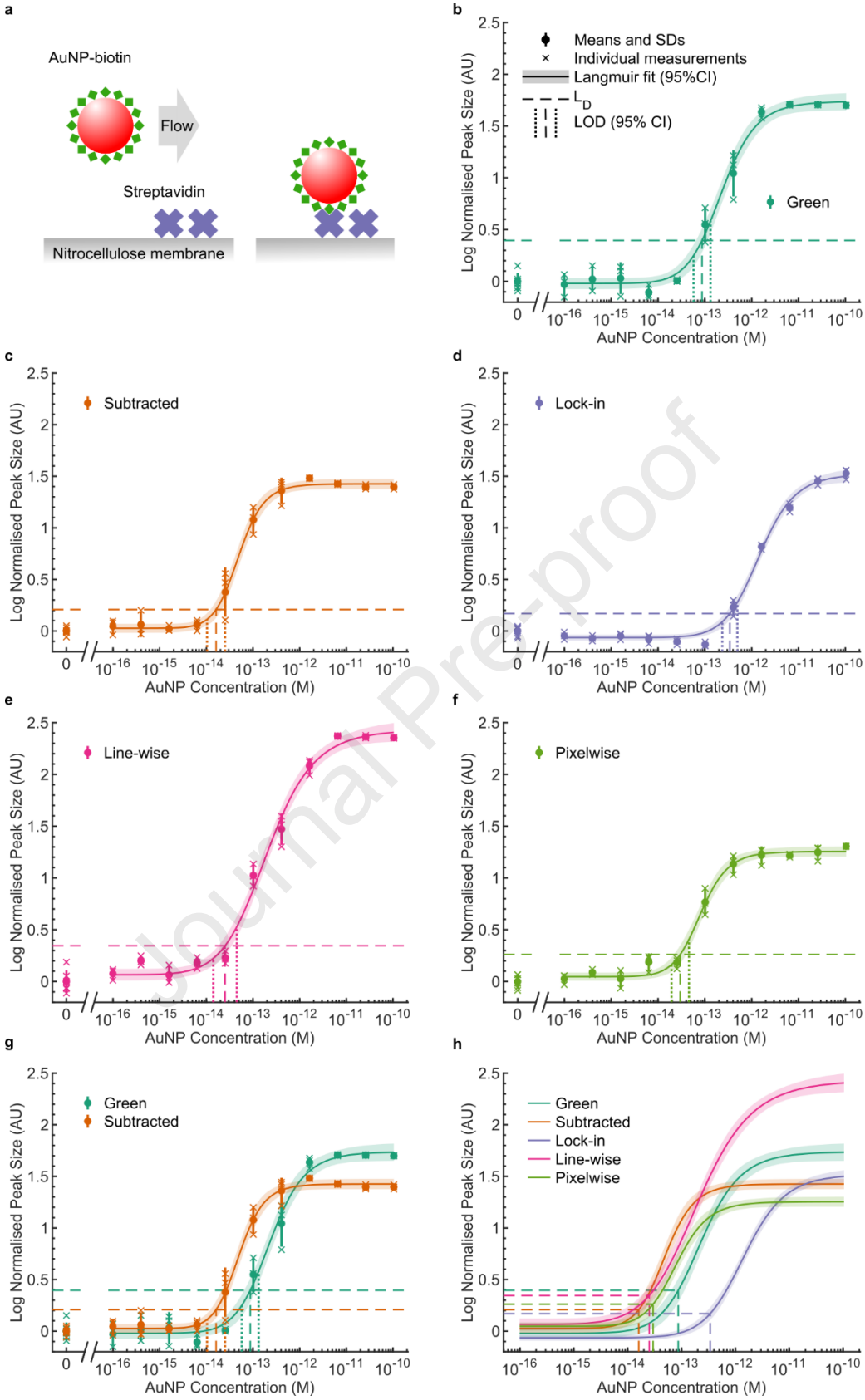

Figure 2: Fundamental LODs for 50 nm AuNPs on LFAs, using a model biotin-avidin interaction with five data capture methods. ***a*** *A schematic of the assay: 50 µL suspensions of biotin-functionalised AuNPs were run at different concentrations on poly-streptavidin-functionalised LFAs, binding directly at the test line. Strips were subsequently imaged and quantified using five methods:* ***b*** *imaging under green (525 nm) illumination, then averaging across the strip width in the normalised image to generate a line profile. The peak height gives the test line intensity. This*

method was used as the gold standard in this work; ***c*** *a subtraction of normalised images taken under green and red (660 nm) illumination, analysed as in* ***b****;* ***d*** *taking an image sequence under 5 Hz wavelength-modulated illumination (see Figure 1c), and applying a lock-in algorithm to the mean of each frame of the sequence to quantify the amplitude at 5 Hz of the resulting absorption signal;* ***e*** *averaging each frame across the width of the test strip to generate a 2-dimensional time-series of line profiles, then applying the lock-in algorithm to each point of the line profile to generate an 'enhanced line profile'. This profile is then analysed as in* ***b****;* ***f*** *applying the lock-in algorithm to each pixel of the image sequence to generate an 'enhanced image', which is then quantified as in* ***b****. The resulting dilution series are plotted in* ***b****-****f*** *(circles show means, with standard deviations and crosses show individual measurements; n=6 for negative controls, n=3 for positives) and fitted to 4PL curves (Supplementary Equation 12), shown as solid lines, with 95% confidence intervals shaded. LODs for each were then calculated using a modified version of the method outlined by Holstein et al.* (Holstein et al., 2015) *(see Materials and Methods). Dashed lines show the cut-offs and LODs, and dotted lines show the 95% confidence intervals of the LODs. LODs and confidence intervals are also listed in Supplementary Table 1.* ***g*** *The best LOD was achieved using the subtraction method in* ***c****, so this dilution series was plotted against the green illumination (****b****, used as the gold standard), giving LODs of 16 and 87 fM, respectively, a 5.4-fold improvement.* ***h*** *The 4PL fits for all five capture methods are plotted along with cut-offs and LODs.*

3.2 Comparison of different nanoparticles

Having chosen a data capture method, the sensitivity of three different plasmonic nanoparticles were tested. 50 nm AuNPs (used previously) were first compared with 100 nm AuNPs as larger particles have a higher absorption per particle (Khlebtsov et al., 2019), so should give a better LOD. Supplementary Figure 8 shows the dilution series for 100 nm AuNPs for the five data capture methods, with LODs summarised in Supplementary Table 4. Again, the subtraction method gives the best LOD, with other background subtraction methods following the same order as with 50 nm AuNPs, although the improvement is reduced across all methods (3.5-fold for subtraction compared to 5.4-fold with 50 nm AuNPs). The wider absorption peak of the larger particles, shown in Supplementary Figure 9, leads to increased relative absorption in the red channel, so reduces the improvement. Increasing AuNP size beyond this leads to absorption peak broadening (Cytodiagnostics, n.d.; Link and El-Sayed, 1999) reducing the peak absorption, and limiting their use for improving LOD. To generate a much larger particle, whilst maintaining the narrow plasmonic peak, a composite particle was designed, comprising a 500 nm polystyrene core decorated with 15 nm AuNPs (530 nm PS-AuNPs), as shown in Figure 1a (right-most particle). The AuNP decoration density was tuned to maximise AuNPs per bead, whilst maintaining adequate separation to retain the plasmonic peak. Additionally, the large particle size can be beneficial for reaction kinetics, as there are more binding sites per particle (Gasperino et al., 2018).

Dynamic light scattering is shown in Figure 3a, showing a monodisperse population. Figure 3b and Supplementary Figure 9 show the absorption spectra of the three particle-types in solution and immobilised on nitrocellulose: there is some peak broadening in the PS-AuNPs due to plasmon coupling of the 15 nm AuNPs (in close proximity), as well as the addition of the broad absorption resulting from the large PS core. Figure 3c-d show transmission electron micrographs of these composite particles, showing the even distribution of AuNPs over the surface of the PS beads. Monodipsersity was also shown using fluorescence microscopy (Supplementary Figure 10 and Supplementary Video).

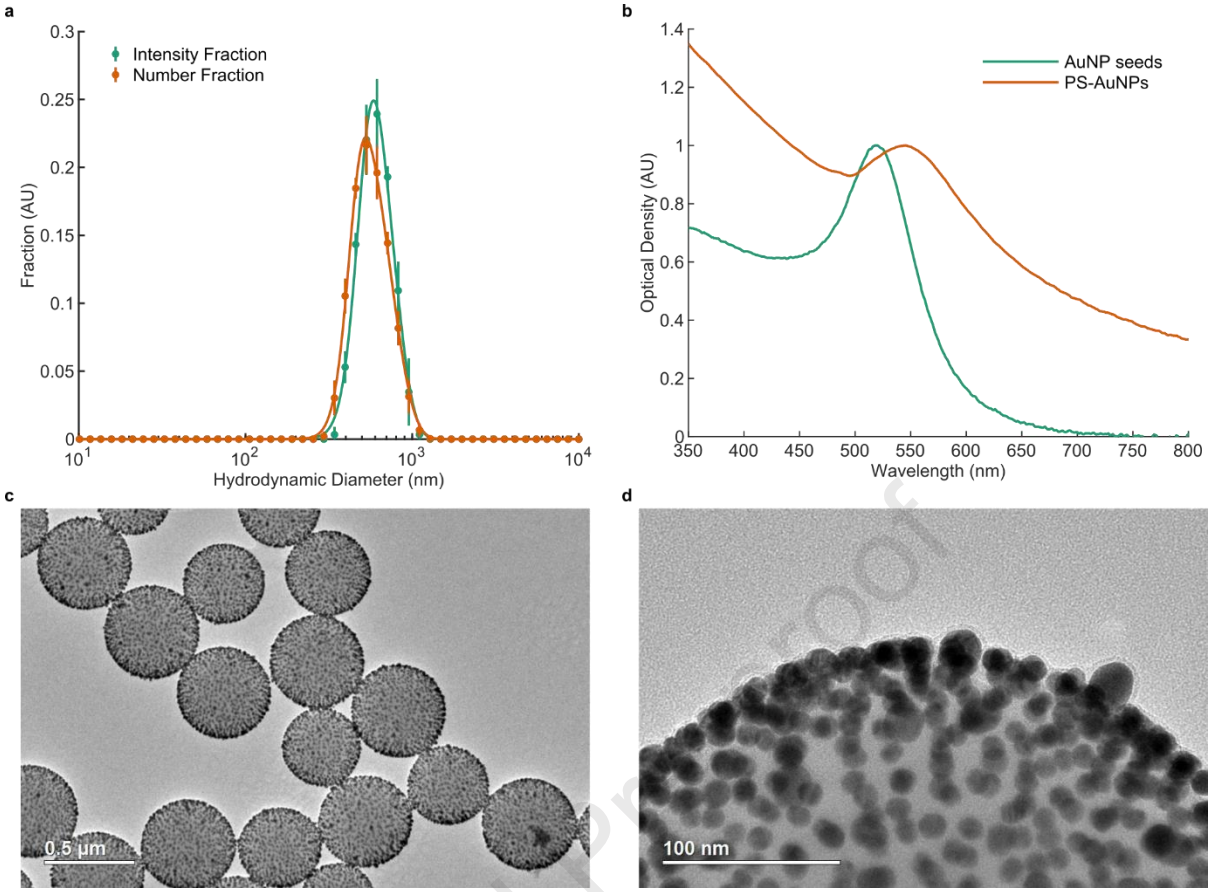

Figure 3: Characterisation of 500 nm polystyrene beads decorated with 15 nm AuNPs (PS-AuNPs). ***a*** *Dynamic light scattering of 530 nm polymer-AuNP composite particles (n=3). This gives a mean polydispersity index of 0.049; a Z-average of 586 nm; and intensity and number means of 617 and 582 nm, respectively. Intensity and number plots were fitted to the skewed exponential:* $N(x) = \frac{exp\left(\frac{-(x-\mu)^2}{2\sigma^2}\right)\text{erfc}\left(\frac{-\alpha(x-\mu)}{\sqrt{2}\sigma}\right)}{\sqrt{2\pi}\sigma}$*, plotted here, to find the peak diameters, giving 584 and 528 nm, respectively. These numbers are all within the expected range of hydrodynamic diameter.* ***b*** *Comparison of absorption spectra for PS-AuNPs and the AuNP seeds. A small blueshift and broadening of the plasmonic peak can be seen in the PS-AuNPs, as well as the addition of the broadband absorbance of the large PS core.* ***c*****-*****d*** *Transmission electron micrographs of the PS-AuNPs, showing the distribution of AuNPs (dark colour) on the surface of the PS beads (lighter colour).*

A comparison of the three particles is shown in Figure 4 giving LODs of 87, 18 and 4.2 fM, for 50 nm AuNPs, 100 nm AuNPs, and 530 nm PS-AuNPs, respectively, under green illumination; and 16, 5.1 and 1.7 fM using subtraction. Supplementary Table 5 shows all three improvements are significant (p-values $<10^{-6}$). ANOVA with Turkey HSD post-hoc tests gives significant differences between all three particle types with p-values of $2.9\text{x}10^{-8}$, $1.3\text{x}10^{-15}$ and $7.1\text{x}10^{-13}$ for green illumination, and $5.2\text{x}10^{-7}$, $1.4\text{x}10^{-15}$ and $8.7\text{x}10^{-10}$ for the subtraction method.

The best improvement is given by the 50 nm AuNPs (5.4-fold), followed by the 100 nm AuNPs (5.4-fold), then the 530 nm PS-AuNPs (2.5-fold). The increased absorption of the PS-AuNPs under red illumination due to the broad absorption of the polystyrene beads and peak broadening of the decorate AuNPs shown in Supplementary Figure 9 accounts for this difference. This is reflected in Supplementary Table 6, where the ratio of green to red absorption for the PS-AuNPs is 5-fold lower. Example normalised images under green and subtracted illumination are shown in Figure 4b and d, respectively. The smoothing and reduction of background variation allows the test line to be visible at lower concentrations. Vignetting seen in the green illumination images is also removed by this

method, as well as artefacts such as dust or dark spots, useful in environments where there is lower uniformity of the lighting, or visual contamination of the strip.

The PS-AuNPs give the best LOD in both green illumination and subtracted methods. The combination of the PS-AuNPs with background removal gives an overall LOD improvement of 58-fold, a scale that would be very difficult to achieve by adapting the binding molecules or assay design. In contrast to simple AuNPs, where there is a fundamental limit at ~100 nm, this composite approach allows future further improvements by adapting the particles, as modelled in Supplementary Figure 11 and Supplementary Discussion. The LOD can be improved by using larger nanoparticles to decorate the polystyrene core particles, and larger polystyrene core could be used (increasing the number of nanoparticles per bead). Nanoparticle form can be tuned to higher OD per area taken on the surface of the bead, such as gold nanorods or silver nanoparticles. This approach can also be used to tune the absorption peak wavelength to match the optical sensor, sample or substrate used to maximise sensitivity for specific applications. For example, silver nanoparticles absorb strongly in the blue region, more optimal for a mobile phone camera Bayer filter due to the greater separation between the blue and red channel spectra than between green and red. The magnitude of the improvement using subtraction over green illumination should scale with the difference in total absorption under the two illuminations. These values are shown in Supplementary Table 6, giving, as expected, the best normalised difference with the 50 nm AuNPs, followed by the 100 nm AuNPs, then the PS-AuNPs.

Reproducibility of the capture methods was investigated by calculating individual LODs for each of three measurement replicates of the same dilution series (Supplementary Figure 12 and Supplementary Table 7). Comparing individual measurement replicates to the full dataset gave non-significant p-values ($0.14 < p < 0.99$), indicating that the capture methods are reproducible.

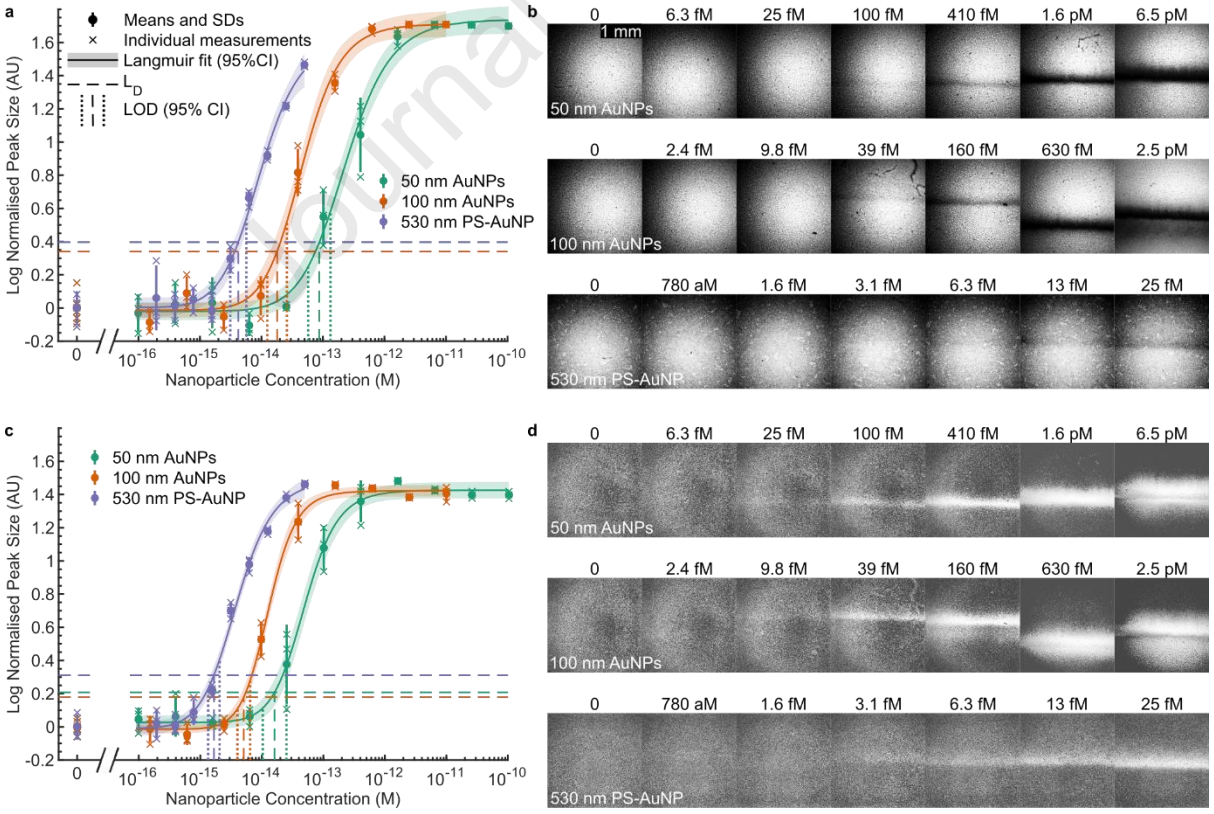

Figure 4: Comparison of different nanoparticles. LODs using three different nanoparticles measured with the model biotin-avidin interaction, as shown in Figure 2a. ***a*** *A comparison of the three nanoparticles, 50 nm AuNPs, 100 nm AuNPs, and 500 nm polystyrene beads decorated with 15 nm AuNPs (530 nm PS-AuNPs), under green (525 nm)*

*illumination. Serial dilutions are plotted as circles with their respective means and standard deviations (AuNPs: n=6 for negative controls, n=3 for positives; and PS-AuNPs: n=9), crosses showing individual points, and 4PL fits (Supplementary Equation 12) plotted as lines with shaded 95% confidence intervals. This gives LODs of 87, 18 and 4.2 fM for 50 nm AuNPs, 100 nm AuNPs, and 530 nm PS-AuNPs, respectively. Example normalised images are shown in **b**. **c** A comparison of the same three nanoparticles measured using the normalised subtraction of images taken with green (525 nm) and red (660 nm) illumination. This gives LODs of 16, 5.1 and 1.7 fM for 50 nm AuNPs, 100 nm AuNPs, and 530 nm PS-AuNPs, respectively. Example normalised, subtracted images are shown in **d**. The removal of vignetting and contaminants (seen in **b**) is demonstrated by these subtracted images.*

3.3 Antigen detection: HIV capsid protein

To demonstrate the two-part approach of composite particles with background subtraction in a real assay, PS-AuNP composite particles were used to detect the HIV capsid protein in model serum (Gray et al., 2018), as shown in Figure 5a. Figure 5b shows the resulting plot of the strips, using both green illumination and subtraction capture methods, giving LODs of 350 and 170 fM, respectively, a 2.0-fold improvement, similar to the improvement measured using the biotin-avidin model (Figure 4, Supplementary Table 5). Due to larger variances, the p-value for the improvement here is 2.2×10^{-1}, however combining the two p-values gives 3.4×10^{-5} and 2.5×10^{-4} using Fisher's combined probability test and a weighted Z-test, respectively, suggesting the improvement is significant. As discussed, there is further scope for future improvements to these composite particles. A comparison with other published LFA-based p24 assays is shown in Supplementary Table 8.

Figure 5c shows green illumination and subtracted images for these p24 strips. Due to the lower-affinity binding components compared to biotin-avidin (Loynachan et al., 2018), the test lines are wider and more uniform (Zhan et al., 2017), so a larger number of pixels was averaged to find the peak size (Supplementary Figure 7d).

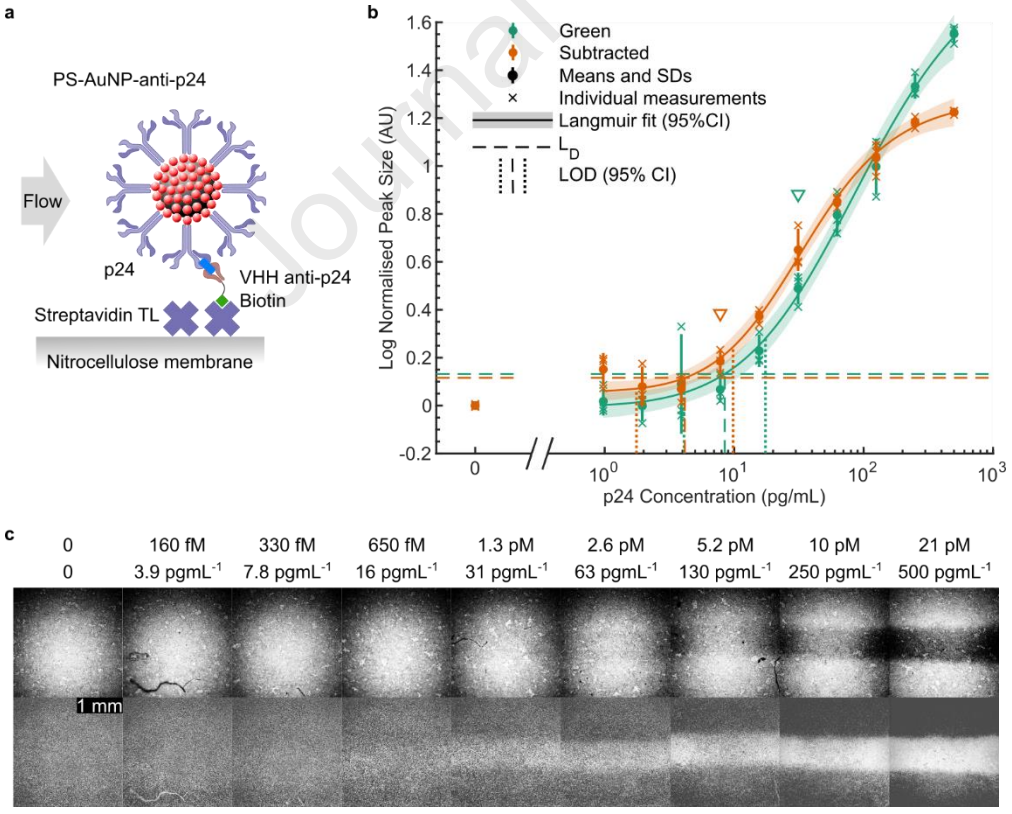

*Figure 5: Detection of the HIV capsid protein, p24. **a** A schematic of the assay: p24-containing samples are mixed with 530 nm PS-AuNPs conjugated with anti-p24 antibodies, and biotinylated VHH anti-p24 (variable domain of camelid heavy-chain-only antibody), forming a sandwich complex. This complex is then run on LFAs, where the biotin-modification binds to a poly-streptavidin test line. **b** A dilution series of p24 was run of LFAs, and imaged with*

both green and red illumination (n=3). A comparison of the green and subtracted methods is plotted here, giving LODs of 350 and 170 fM (8.5 and 4.2 pg/mL), respectively, a 2.0-fold improvement. Inverted triangles mark the lowest measured concentration that is significantly different from the negative controls for each capture method: 31 and 7.8 pg/mL, by ANOVA. ***c*** *Example images of both green illumination and subtracted images of the p24 LFA dilution series. These images also demonstrate the removal of vignetting and contamination, as previously, particularly evident in the 160 fM images, where the impact of two fibrous contaminants is greatly reduced.*

A user-friendly, open-source software tool was developed. The tool can be used to fit LODs to data using the three models described herein, plot single and multiple-dataset graphs, and perform two-tailed t-tests to compare LODs, as shown in Supplementary Figure 13.

4 Conclusions

Here we have shown that a range of simple background removal methods using two illumination wavelengths can give 2.0-5.4-fold improvements in LOD of plasmonic nanoparticle-based LFAs, depending on the ratios of the absorption at the two wavelengths. In contrast to other methods, this technique requires no modifications to existing LFAs using plasmonic nanoparticles, and indeed the strips can continue to be read by eye, adding a reader if available, conveying an improved LOD, for example to verify negatives and weak positives. This improvement in LOD gives, in turn, the same improvement in the dynamic range by quantifying images before and after subtraction. These analysis methods could be performed using a standard lateral flow reader, or smartphone camera using either a dedicated attachment (Mudanyali et al., 2012) using specific LEDs, or ambient light, filtered with the camera's Bayer filter. This would allow these methods to be used in a variety of settings including low-resource or point-of-care settings.

Combining with composite PS-AuNP particles gave a further 11-fold improvement in sensitivity over for a total improvement in sensitivity of 58-fold over 50 nm AuNPs under green illumination, without adding assay steps. This gave LODs of 1.7 fM with a biotin-avidin model, and 170 fM (4.2 pg/mL) for the detection of an HIV antigen. The combination of background subtraction with these highly-tuneable composite particles allows for optimised assays suiting a variety of formats and sensors. Background subtraction could also in future be used with enzymatic LFAs (Loynachan et al., 2018), when generating a chromogen with a sharp absorption peak.

5 Acknowledgements

This work was funded by the i-sense EPSRC IRC in Early Warning Sensing Systems for Infectious Diseases (EP/K031953/1), including an i-sense Mobility Fellowship for work at UCLA; and i-sense EPSRC IRC in Agile Early Warning Sensing Systems in Infectious Diseases and Antimicrobial Resistance (EP/R00529X/1); National Science Foundation PATHS-UP; Royal Society Wolfson Research Merit Award to R.A.M. (WM130111); LCN Departmental Studentship to B.S.M.; UK Biotechnology and Biological Sciences Research Council and AstraZeneca for the Industrial CASE PhD studentship for M.B. is gratefully acknowledged (BB/V509607/1); Y.C. acknowledges support from the Chinese Scholarship Council.

6 CRediT authorship contribution statement

Benjamin S. Miller: conceptualization of the study, experimental planning, carrying out lateral flow and imaging experiments, data analysis. **Michael R. Thomas:** conceptualization of the study, experimental planning, carrying out lateral flow and particle conjugation experiments, data analysis. **Matthew Banner:** data analysis. **Jeongyun Kim:** carrying out particle conjugation experiments. **Yiyun**

Chen: experimental planning, carrying out particle conjugation experiments, TEM and DLS characterisation. **Qingshan Wei:** conceptualization of the study, experimental planning, data analysis. **Derek K. Tseng:** conceptualization of the study, device design. **Zoltán S. Göröcs:** conceptualization of the study, experimental planning. **Aydogan Ozcan:** conceptualization of the study, data analysis. Molly **M. Stevens:** conceptualization of the study, experimental planning. **Rachel A. McKendry:** conceptualization of the study, experimental planning, data analysis.

7 Bibliography

Bond, M., Elguea, C., Yan, J.S., Pawlowski, M., Williams, J., Wahed, A., Oden, M., Tkaczyk, T.S., Richards-Kortum, R., 2013. Lab on a Chip 13, 2381. https://doi.org/10.1039/c3lc40908b

Brewer, C.A., 2021ColorBrewer: Color Advice for Maps [WWW Document]. URL https://colorbrewer2.org/# (accessed 5.24.21).

Buitrago-Garcia, D., Egli-Gany, D., Counotte, M.J., Hossmann, S., Imeri, H., Ipekci, A.M., Salanti, G., Low, N., 2020. PLoS Medicine 17, e1003346. https://doi.org/10.1371/journal.pmed.1003346

Choi, D.H., Lee, S.K., Oh, Y.K., Bae, B.W., Lee, S.D., Kim, S., Shin, Y.-B., Kim, M.-G., 2010. Biosensors and Bioelectronics 25, 1999–2002. https://doi.org/10.1016/j.bios.2010.01.019

Cobeldick, S., 2021ColorBrewer: Attractive and Distinctive Colormaps [WWW Document]. URL https://github.com/DrosteEffect/BrewerMap (accessed 5.26.21).

Cytodiagnostics, Gold Nanoparticle Properties - Cytodiagnostics [WWW Document]. URL http://www.cytodiagnostics.com/store/pc/Gold-Nanoparticle-Properties-d2.htm (accessed 11.19.18).

Danz, A., 2021copyUIAxes [WWW Document]. URL https://uk.mathworks.com/matlabcentral/fileexchange/73103-copyuiaxes?s_tid=srchtitle (accessed 5.26.21).

Dunn, J., Wild, D., 2013, in: Wild, D. (Ed.), The Immunoassay Handbook (Fourth Edition). Elsevier, Oxford, pp. 323–336. https://doi.org/https://doi.org/10.1016/B978-0-08-097037-0.00022-1

Edelstein, A.D., Tsuchida, M.A., Amodaj, N., Pinkard, H., Vale, R.D., Stuurman, N., 2014. Journal of Biological Methods 1, 10. https://doi.org/10.14440/jbm.2014.36

Evans, E., Moreira Gabriel, E.F., Benavidez, T.E., Tomazelli Coltro, W.K., Garcia, C.D., 2014. Analyst 139, 5560–5567. https://doi.org/10.1039/c4an01147c

Fu, E., Liang, T., Spicar-Mihalic, P., Houghtaling, J., Ramachandran, S., Yager, P., 2012. Analytical Chemistry 84, 4574–4579. https://doi.org/10.1021/ac300689s

Gasperino, D., Baughman, T., Hsieh, H. V., Bell, D., Weigl, B.H., 2018. Annual Review of Analytical Chemistry 11, annurev-anchem-061417-125737. https://doi.org/10.1146/annurev-anchem-061417-125737

Gray, E.R., Bain, R., Varsaneux, O., Peeling, R.W., Stevens, M.M., McKendry, R.A., 2018. AIDS 32, 2089–2102. https://doi.org/10.1097/QAD.0000000000001982

Holstein, C.A., Griffin, M., Hong, J., Sampson, P.D., 2015. Analytical Chemistry 87, 9795–9801. https://doi.org/10.1021/acs.analchem.5b02082

Hu, J., Wang, L., Li, F., Han, Y.L., Lin, M., Lu, T.J., Xu, F., 2013. Lab on a Chip 13, 4352. https://doi.org/10.1039/c3lc50672j

Huang, Xiaolin, Song, J., Yung, B.C., Huang, Xiaohua, Xiong, Y., Chen, X., 2018. Chemical Society Reviews 47, 2873–2920. https://doi.org/10.1039/C7CS00612H

Khlebtsov, B.N., Tumskiy, R.S., Burov, A.M., Pylaev, T.E., Khlebtsov, N.G., 2019. ACS Applied Nano Materials 2, 5020–5028. https://doi.org/10.1021/acsanm.9b00956

Laitinen, M.P.A., Vuento, M., 1996. Biosensors and Bioelectronics 11, 1207–1214. https://doi.org/10.1016/0956-5663(96)88085-7

Link, S., El-Sayed, M. a., 1999. The Journal of Physical Chemistry B 103, 4212. https://doi.org/10.1021/jp984796o

Loynachan, C.N., Thomas, M.R., Gray, E.R., Richards, D.A., Kim, J., Miller, B.S., Brookes, J.C., Agarwal, S., Chudasama, V., McKendry, R.A., Stevens, M.M., 2018. ACS Nano 12, 279–288. https://doi.org/10.1021/acsnano.7b06229

May, M., Gompels, M., Delpech, V., Porter, K., Post, F., Johnson, M., Dunn, D., Palfreeman, A., Gilson, R., Gazzard, B., Hill, T., Walsh, J., Fisher, M., Orkin, C., Ainsworth, J., Bansi, L., Phillips, A., Leen, C., Nelson, M., Anderson, J., Sabin, C., 2011. BMJ 343, d6016–d6016. https://doi.org/10.1136/bmj.d6016

Miller, B.S., 2019, Connected paper microfluidics: from quantitative biochemical analysis to ultrasensitive nanodiamond diagnostics. (unknown).

Miller, B.S., Bezinge, L., Gliddon, H.D., Huang, D., Dold, G., Gray, E.R., Heaney, J., Dobson, P.J., Nastouli, E., Morton, J.J.L., McKendry, R.A., 2020. Nature 587, 588–593. https://doi.org/10.1038/s41586-020-2917-1

Mudanyali, O., Dimitrov, S., Sikora, U., Padmanabhan, S., Navruz, I., Ozcan, A., 2012. Lab on a Chip 12, 2678–2686. https://doi.org/10.1039/c2lc40235a

Ngom, B., Guo, Y., Wang, X., Bi, D., 2010. Analytical and Bioanalytical Chemistry 397, 1113–1135. https://doi.org/10.1007/s00216-010-3661-4

Rivas, L., de la Escosura-Muñiz, A., Serrano, L., Altet, L., Francino, O., Sánchez, A., Merkoçi, A., 2015. Nano Research 8, 3704–3714. https://doi.org/10.1007/s12274-015-0870-3

Rodríguez, M.O., Covián, L.B., García, A.C., Blanco-López, M.C., 2016. Talanta 148, 272–278. https://doi.org/10.1016/j.talanta.2015.10.068

Ruiz-Sanchez, A.J., Parolo, C., Miller, B.S., Gray, E.R., Schlegel, K., McKendry, R.A., 2017. Journal of Materials Chemistry B 5, 7262–7266. https://doi.org/10.1039/c7tb01394a

Shah, K.G., Singh, V., Kau, P.C., Abe, K., Yager, P., 2018. https://doi.org/10.1021/acs.analchem.8b01241

't Lam, R.U.E., 2010. Analytica Chimica Acta 659, 68–84. https://doi.org/10.1016/j.aca.2009.11.032

Tang, D., Sauceda, J.C., Lin, Z., Ott, S., Basova, E., Goryacheva, I., Biselli, S., Lin, J., Niessner, R., Knopp, D., 2009. Biosensors and Bioelectronics 25, 514–518. https://doi.org/10.1016/j.bios.2009.07.030

The University of Liverpool, 2020Liverpool Covid-19 Community Testing Pilot.

The World Bank, 2020, The Global Economic Outlook During the COVID-19 Pandemic: A Changed World [WWW Document]. URL https://www.worldbank.org/en/news/feature/2020/06/08/the-global-economic-outlook-during-the-covid-19-pandemic-a-changed-world (accessed 1.7.21).

Trujillo-Ortiz, A., 2021agtlaminv - File Exchange - MATLAB Central [WWW Document]. URL https://uk.mathworks.com/matlabcentral/fileexchange/45943-gtlaminv (accessed 5.26.21).

Trujillo-Ortiz, A., 2021bgtlamtest [WWW Document]. URL https://uk.mathworks.com/matlabcentral/fileexchange/52436-gtlamtest?s_tid=srchtitle (accessed 5.26.21).

UNAIDS, 2020, Global HIV & AIDS statistics — 2020 fact sheet [WWW Document]. URL https://www.unaids.org/en/resources/fact-sheet (accessed 1.7.21).

Wang, Y., Qin, Z., Boulware, D.R., Pritt, B.S., Sloan, L.M., González, I.J., Bell, D., Rees-Channer, R.R., Chiodini, P., Chan, W.C.W., Bischof, J.C., 2016. Analytical Chemistry 88, 11774–11782. https://doi.org/10.1021/acs.analchem.6b03406

World Health Organization, 2021WHO Coronavirus Disease (COVID-19) Dashboard [WWW Document]. URL https://covid19.who.int/ (accessed 1.7.21).

World Health Organization, 2012WHO | Low-cost tools for diagnosing and monitoring HIV infection in low-resource settings [WWW Document]. Bulletin of the World Health Organization. URL http://www.who.int/bulletin/volumes/90/12/BLT-12-102780-table-T1.html (accessed 8.14.15).

Zhan, L., Guo, S., Song, F., Gong, Y., Xu, F., Boulware, D.R., McAlpine, M.C., Chan, W.C.W., Bischof, J.C., 2017. Nano Letters 17, 7207–7212. https://doi.org/10.1021/acs.nanolett.7b02302

Highlights

Sub-picomolar lateral flow antigen detection with two-wavelength imaging of composite nanoparticles

Benjamin S. Miller, Michael R. Thomas, Matthew Banner, Jeongyun Kim, Brian Chen, Qingshan Wei, Derek K. Tseng, Zoltán S. Göröcs, Aydogan Ozcan, Molly M. Stevens, Rachel A. McKendry

- Background removal to improve the sensitivity of absorption-based lateral flow tests.
- Two-wavelength imaging conveys 5.4-fold improvement with gold nanoparticles.
- Composite polymer beads decorated with gold nanoparticles improve sensitivity.
- Combined 58-fold improvement over 50 nm gold nanoparticles with conventional imaging.
- Application to HIV capsid protein detection gives 170 fM limit of detection.

Declaration of interests

☒ The authors declare that they have no known competing financial interests or personal relationships that could have appeared to influence the work reported in this paper.

☐The authors declare the following financial interests/personal relationships which may be considered as potential competing interests: